The effect of lithology on the relationship between denudation rate and chemical weathering pathways

Aaron Bufe[1], Kristen L. Cook[1], Albert Galy[2], Hella Wittmann[1], Niels Hovius[1,3]

[1]German Research Center for Geosciences, Potsdam 14473, Germany
5   [2]Centre de Recherches Pétrographiques et Géochimiques, CNRS, Université de 13 Lorraine, 54500 Nancy, France.
[3]Institute of Geosciences, Potsdam University, Potsdam 14476, Germany

Correspondence to: Aaron Bufe (aaronbufe@gmail.com)

Abstract. The denudation of rocks in mountain belts exposes a range of fresh minerals to the surface of the Earth that are
10   chemically weathered by acidic and oxygenated fluids. The impact of the resulting coupling between denudation and weathering rates fundamentally depends on the types of minerals that are weathering. Whereas silicate weathering sequesters CO_2, the combination of sulfide oxidation and carbonate dissolution emits CO_2 to the atmosphere. Here, we combine the concentrations of dissolved major elements in stream waters with ^{10}Be basin-wide denudation rates from 35 small catchments in eastern Tibet to elucidate the importance of lithology in modulating the relationships between denudation rate,
15   chemical weathering pathways, and CO_2 consumption or release. Our catchments span three orders of magnitude in denudation rate in low-grade flysch, high grade metapelites, and granitoid rocks. For each stream, we estimate the concentrations of solutes sourced from silicate weathering, carbonate dissolution, and sulfide oxidation using a mixing model. We find that for all lithologies, cation concentrations from silicate weathering are largely independent of denudation rate, but solute concentrations from carbonates and, where present, sulfides increase with increasing denudation rate. With
20   increasing denudation rates, weathering may, therefore, shift from consuming to releasing CO_2 in both (meta)sedimentary and granitoid lithologies. We find that catchments draining high grade metamorphic rocks have systematically higher concentrations of sulfate from sulfide weathering than catchments containing weakly metamorphosed sediments. Moreover, our data provide tentative evidence that sulfate concentrations in these catchments are potentially more sensitive to denudation rate. We propose that changes in the sulfur oxidation state during prograde metamorphism of pelites in the mid-
25   crust could lead to sulfate reduction that is even more complete than in low-grade sediments and provides a larger sulfide source for oxidation upon re-exposure of the rocks. In this case, the elevated concentration of sulfate in catchments draining high-grade metapelites would suggest that exposure of an increasing fraction of metamorphic rocks during orogenesis could lead to a boost in the release of CO_2 that is independent of denudation rate.

1 Introduction

30

The relationship between chemical weathering and CO_2 drawdown modulates the global carbon cycle and Earth's climate (Walker et al., 1981; Berner et al., 1983). Uplift and denudation of rock control the supply of unweathered minerals to the surface of the Earth and impact the residence time of these minerals in the weathering zone (e.g. Hilley et al., 2010; West et al., 2005; Gabet and Mudd, 2009; Riebe et al., 2001). Thus, increases in denudation rates can boost chemical weathering and

35 ultimately affect Earth's climate (Raymo and Ruddiman, 1992; Hilton and West, 2020; Caves Rugenstein et al., 2019; Kump and Arthur, 1997). The impact of chemical weathering on the attendant emission or drawdown of CO_2 depends on the relative importance of different weathering pathways (Torres et al., 2016; Torres et al., 2014; Calmels et al., 2007; Bufe et al., 2021; Hilton and West, 2020; Berner et al., 1983; Hartmann et al., 2009). Weathering of silicate minerals by carbonic acid consumes CO_2 from the atmosphere and drives the sequestration of this carbon into marine carbonates (Walker et al.,

40 1981). In turn, sulfuric acid produced by the oxidation of pyrite can drive rapid dissolution of carbonate minerals that releases CO_2 into the atmosphere (Calmels et al., 2007; Das et al., 2012; Torres et al., 2014). Weathering of silicate minerals by sulfuric acid and of carbonate minerals by carbonic acid are carbon neutral (Calmels et al., 2007). Importantly, carbonates and sulfides weather several orders of magnitude faster than silicate minerals (Lasaga, 1984; Williamson and Rimstidt, 1994; Morse and Arvidson, 2002), such that sulfuric acid-driven carbonate weathering dominates the total solute flux even in

45 lithologies with small fractions of pyrite or carbonate (Anderson et al., 2000; Calmels et al., 2007; Das et al., 2012; Torres et al., 2016; Emberson et al., 2016a; Jacobson and Blum, 2003; Bufe et al., 2021).

The dependence of chemical weathering on mineralogy implies a lithologic control on the balance of CO_2 drawdown and CO_2 release by weathering reactions. Fresh and fine-grained mafic rocks, such as basalts, exhibit some of the fastest silicate weathering rates on the planet and contribute disproportionally to global silicate weathering fluxes (Dessert et al., 2003; Li et

50 al., 2016; Gaillardet et al., 1999). Felsic igneous rocks typically weather more slowly, but silicate weathering in these rocks is also thought to be sensitive to denudation rates (Riebe et al., 2004; West et al., 2005). In contrast, weathering of siliciclastic (meta)sedimentary rocks is often dominated by the dissolution of minor carbonate and sulfides (Anderson et al., 2000; Calmels et al., 2007; Das et al., 2012; Torres et al., 2016; Emberson et al., 2016a; Jacobson and Blum, 2003; Bufe et al., 2021; Blattmann et al., 2019), and rapid denudation and exposure of these rocks can drive CO_2 release from weathering

55 (Calmels et al., 2007; Torres et al., 2016; Torres et al., 2014; Bufe et al., 2021; Märki et al., 2021). Carbonate dissolution also dominates weathering of carbonate-rich sediments (Erlanger et al., 2021; Gaillardet et al., 1999; Gaillardet et al., 2018), but the role of sulfide oxidation and, therefore, the impact of carbonate weathering on the long-term CO_2-cycle can be limited in these rocks (Erlanger et al., 2021; Gaillardet et al., 1999; Gaillardet et al., 2018).

Even though lithology exerts a fundamental control on the link between weathering and Earth's carbon cycle, few studies

60 have directly compared and quantified the impact of lithologic variation on the link between physical denudation and chemical weathering and on the importance of different weathering pathways. Such knowledge is important in the context of mountain building, as ongoing exhumation progressively exposes successions of different lithologies to chemical weathering

(Hilton and West, 2020). Landscape-scale weathering fluxes are typically estimated by measuring the solute concentration and runoff in rivers that integrate water fluxes across the upstream catchment (Gaillardet et al., 1999; Drever and Clow, 2018; Drever and Zobrist, 1992; White and Blum, 1995). In many settings, denudation gradients coincide with gradients in precipitation, temperature, tectonics, biomass, and/or substrate properties such as fracture density or metamorphic grade (Dixon et al., 2016); gradients that affect weathering kinetics independently of denudation rates (Guo et al., 2019; Gaillardet et al., 2018; Ibarra et al., 2016; Godsey et al., 2019; White and Blum, 1995; Drever and Zobrist, 1992; Li et al., 2016; Oeser and Von Blanckenburg, 2020; Uhlig and Von Blanckenburg, 2019). These co-variations can complicate the interpretation of changes in weathering. Here, we investigate the impact of lithologic variations on chemical weathering across a nearly three-order of magnitude wide denudation rate gradient along the eastern margin of the Tibetan Plateau that includes three well-separated groups of lithology (Fig. 1) and relatively small changes in precipitation, elevation, and temperature (Fig. 2, Table S1).

2 Geologic setting

On the eastern Tibetan Plateau west of the Sichuan Basin lies the Songpan-Ganze (or Songpan-Garzê) fold belt, which formed during the late Triassic to early Jurassic closure of part of the Paleotethys ocean (Burchfiel et al., 1995; Weller et al., 2013; Chen et al., 2007). The Songpan-Ganze terrane is characterized by a 5 – 15 km thick sequence of tightly folded Triassic flysch that overlies Paleozoic metasedimentary rocks and Precambrian basement (Roger et al., 2010; Weller et al., 2013) (Fig. 1). These units have been intruded by granitoids during both the Mesozoic and Cenozoic. Reactivation of the region during the Cenozoic Indo-Eurasian collision formed zones of rapid uplift and denudation within and at the eastern edge of the slowly eroding Tibetan plateau. Here, we focus on the southeastern part of the Songpan-Ganze fold belt in the region around the Danba Structural culmination and the zone of rapid uplift centered around Gongga Shan (Fig. 1). In this area, in-situ [10]Be-derived basin-wide denudation rates vary more than 200-fold from 0.018 mm/yr to 7 mm/yr over a distance of 100-200 km (Ouimet et al., 2009; Cook et al., 2018). The region features three principal lithologic groups. Most of the area exposes the Triassic Songpan-Ganze flysch, a sequence of deep sea turbidites that is unmetamorphosed or weakly metamorphosed over large areas but can reach greenschist facies close to Gongga Shan and the Danba Structural culmination (Burchfiel et al., 1995; Chen et al., 2007). The underlying Paleozoic sequence is exposed in the Danba structural culmination and in the Longmen Shan and consists of a passive margin sequence, which has undergone metamorphism up to amphibolite facies (Huang et al., 2003; Weller et al., 2013). Finally, granitic rocks of a range of ages from Precambrian to Cenozoic are exposed throughout the area (Roger et al., 2010; Roger et al., 2004; Searle et al., 2016) (Fig. 1, Table S1). Rocks within each one of these three broad lithologic groups have varying compositions, but the difference in chemical compositions and mineralogy between these three lithologic groups is greater than the variability within each one of the groups (Jiang et al., 2018; Weller et al., 2013; Chen et al., 2007) (Table S3, Fig. 3). Moreover, minor carbonate and sulfide phases occur in varying proportions in these dominantly silicate lithologies (Jiang et al., 2018; Weller et al., 2013; Chen et al., 2007).

95   The region is characterized by a cold and humid climate with a pronounced wet monsoon season during the summer months and drier winter months. Mean annual precipitation rates derived by the Tropical Rainfall Measuring Mission (TRMM) vary ~4-5-fold between 300 – 1340 mm/yr (Bookhagen and Burbank, 2010) (Fig. 2B). This range of precipitation values is very similar to the range of runoff values previously estimated for small catchments around the Gongga Shan (Table 1 in Jiang et al. (2018)). Our sampled catchments fall within a relatively narrow elevation window with catchment averaged elevations of

100   3500-4800 m with three exceptions at lower mean elevations of 2600 – 2800 m (Fig. 2A, Table S1). Neither the elevation, nor the annual precipitation in the studied catchments or the temperature of sampled stream waters correlate strongly with the denudation rate across the area (Fig. 2)

3 Methods

3.1 Sample collection and analysis

105   We collected water samples from 35 small catchments around the region of Mt Gongga and the Danba structural culmination (Fig. 1, Table S1). Water samples were collected in mid-May 2018, prior to the rainy season, over a period of 5 days when all catchments were subject to similar hydrological conditions. Most of the sampled catchments drain a single lithologic group: Thirteen catchments drain the Triassic flysch that is dominantly composed of unmetamorphosed or weakly metamorphosed mixed carbonate-siliciclastic sediments. Only two of the flysch catchments include rocks that have been

110   metamorphosed to garnet-bearing greenschists (S18-35 & S18-36, Fig. 3C). Eleven catchments drain granitic rocks, and six catchments drain high-grade Paleozoic and Precambrian metasedimentary rocks, whereas five catchments drain a mix of granitic rocks and Triassic flysch (Fig. 3C, Table S1). Samples were taken as close to sites sampled for cosmogenic nuclide-derived denudation rates (Cook et al., 2018) as possible, and upstream of potential major anthropogenic influences. Water samples were filtered in situ with single-use 0.2 μm filters and collected in HDPE bottles. Aliquots for cation analysis were

115   acidified on-site to a pH of ~2 with 3M ultrapure HNO_3. Temperature, pH, and conductivity were measured in the field using a WTW Multi 3430 multimeter.

Anion and cation analyses were conducted at the GFZ Potsdam on a Dionex ICS-1100 Ion Chromatograph and a Varian 720 ICP-OES, respectively, following the procedure described in Bufe et al. (2021). The concentration of bicarbonate was estimated by charge balance. Such estimation is reasonable in active mountain settings where organic acids are scarce and

120   estimates of bicarbonate from charge balance are within uncertainty of alkalinity values from titrations (Galy and France-Lanord, 1999). Analytical uncertainties for cation analyses were derived from the largest deviation of the calibration standards from the calibration line. For anions, uncertainty estimates were derived from the standard deviation of three repeat measurements (Table S2).

3.2 Unmixing of solute sources

125 We consider four major sources of cations to rivers in the study area: Silicate weathering, carbonate weathering, cyclic- (assumed to be dominated by wet precipitation), and hotsprings contributions (Table 1). Major evaporites are not reported in the upper Triassic flysch or in the Paleozoic metamorphic rocks around the Danba Structural culmination (Jiang et al., 2018; Chen et al., 2007). Moreover, we assume that secondary precipitation of carbonate minerals is negligible in the area. This assumption is based on the observation that all samples are either undersaturated with respect to calcium carbonate or are

130 within uncertainty of saturation, except for two Flysch basins that suggest slightly super-saturated conditions (Fig. A1).

We used a 4-endmember inverse model to unmix these contributions based on the relative concentration of the three major soluble cations (Na^+, Ca^{2+}, and Mg^{2+}) and chloride (Cl^-) (Bufe et al., 2021; Moon et al., 2014; Gaillardet et al., 1999; Torres et al., 2016). The mixing model requires that each one of the endmembers is unique and, therefore, occupies a range of compositions that is distinct from the composition of other endmembers in the considered space (Fig. 3A-B). In the

135 model, we minimized the following set of equations using the constrained linear least squares solver lsqlin in MATLAB:

$$\left[\frac{X}{Ca^{2+}}\right]_{riv} = \alpha_{Ca,sil}\left[\frac{X}{Ca^{2+}}\right]_{sil} + \alpha_{Ca,carb}\left[\frac{X}{Ca^{2+}}\right]_{carb} + \alpha_{Ca,cy}\left[\frac{X}{Ca^{2+}}\right]_{cy} + \alpha_{Ca,hs}\left[\frac{X}{Ca^{2+}}\right]_{hs},\qquad(1\text{-}3)$$

With $X = Na^+$, $X = Mg^{2+}$, and $X = Mg^{2+}$ (three equations) under the conditions that:

$$\alpha_{Ca,sil} + \alpha_{Ca,carb} + \alpha_{Ca,cy} + \alpha_{Ca,hs} = 1 \qquad(4)$$

and

140 $$0 \leq \alpha_{Ca,sil} \leq 1;\ \ 0 \leq \alpha_{Ca,carb} \leq 1;\ \ 0 \leq \alpha_{Ca,cy} \leq 1;\ \ 0 \leq \alpha_{Ca,hs} \leq 1 \qquad(5)$$

Here, $\left[\frac{X}{Ca^{2+}}\right]$ is the ratio of concentrations of ion X and calcium, and $\alpha_{Ca,Y}$ is the fraction of calcium sourced from endmember Y. The subscripts sil, $carb$, cy, and hs denote contributions from silicate, carbonate, cyclic (precipitation), and hotspring sources respectively and subscript riv denotes the sampled mixed ratio in the river water. For each sample, we input an a-priori estimate of the endmember ratios and their uncertainty (Table 1). We then randomly picked a set of four

145 endmembers from a normal distribution with mean and standard deviation defined by the a-priori endmember estimate and its uncertainty. For each of 100,000 iterations, we used a reduced chi-squared statistic to estimate the goodness of fit based on the sum of (1) the squared distances between the modelled and sampled $\left[\frac{X}{Ca^{2+}}\right]$-ratios normalized by the variance in the samples, and (2) the squared distances between the randomly picked endmember $\left[\frac{X}{Ca^{2+}}\right]$-ratios and the mean input value normalized by the variance of the input. The set of endmembers and corresponding fractions, α_{Ca}, with the lowest misfit

150 were chosen as model output, whereas the uncertainty was estimated based on the standard deviation of all Monte Carlo runs, excluding those runs with reduced chi-squared distances of more than four (i.e. models with average distances of more than twice the uncertainty range of the input parameters).

The most important parameters in the mixing model are the endmember estimates (Table 1). Both, silicate and carbonate endmembers are based on compiled bedrock compositions around the study area (Jiang et al., 2018; Weller et al., 2013;

155 Chen et al., 2007) (Table S3) as well as the assumption that: $\left[\frac{Cl^-}{Ca^{2+}}\right]_{sil} = \left[\frac{Cl^-}{Ca^{2+}}\right]_{carb} = \left[\frac{Na^+}{Ca^{2+}}\right]_{carb} = 0$. Published bulk rock analyses of rocks in the region show a substantial variability. Nevertheless, samples from the three individual lithologic groups (granitoids, Paleozoic passive margin metapelites and Triassic flysch) form distinct trends in $Mg^{2+}/Ca^{2+} - Na^+/Ca^{2+}$ space (Fig. 3A-B). The composition of the granitoids varies around the global silicate endmember estimated from small streams that drain pure silicate lithologies (Gaillardet et al., 1999; Burke et al., 2018). Compared to the granites, the

160 Paleozoic metapelites are substantially enriched in magnesium and the flysch rocks are characterized by high calcium contents (Fig. 3A-B). Major carbonate phases are not reported in the Paleozoic metapelites (Weller et al., 2013) and in the granitoids (Jiang et al., 2018). Even if trace carbonate minerals can strongly affect solutes sourced from chemical weathering (Blum et al., 1998; Jacobson and Blum, 2003; Anderson et al., 2000; Emberson et al., 2016a), we assume that the bulk-rock geochemistry measurement are affected only negligibly. Thus, the mean and standard deviation of the bulk rock analyses are

165 dominated by and representative of the silicate endmember from these lithologies (Table 1). In turn, the flysch samples contain 4% – 80% carbonate that occurs both as calcite minerals and as carbonate cement (Chen et al., 2007). Therefore, these samples represent a mix between a carbonate and a silicate endmember (Fig. 3B). Based on two sediment samples with the highest carbonate content and zero sodium (Table S3), we estimated the magnesium content of carbonates in the area to $\left[\frac{Mg^{2+}}{Ca^{2+}}\right]_{carb} = 0.04^{+0.13}_{-0.04}$ which is consistent with the absence of reported dolomite in the area (Chen et al., 2007). The error in

170 this estimate is from the 68% confidence band of a regression through all flysch samples with a fixed intercept at $\left[\frac{Na^+}{Ca^{2+}}\right]_{sil} = 0$ and $\left[\frac{Mg^{2+}}{Ca^{2+}}\right]_{carb} = 0.04$ and assuming $\left[\frac{Mg^{2+}}{Ca^{2+}}\right]_{carb} \geq 0$ (Fig. A1B). Based on knowledge of the carbonate endmember, $\left[\frac{Mg^{2+}}{Ca^{2+}}\right]_{carb}$, and the carbonate content of the samples $\langle (Ca, Mg)_{0.5} CO_3 \rangle$ (where square brackets denote the concentration in weight percent), the $\left[\frac{Na^+}{Ca^{2+}}\right]_{sil}$ ratio of the flysch is given as:

$$\left[\frac{Na^+}{Ca^{2+}}\right]_{sil} = \frac{\langle Na \rangle_{riv}}{(\langle Ca \rangle_{riv} - \langle Ca \rangle_{carb})} \frac{u_{Ca}}{u_{Na}} \tag{6}$$

175 where

$$\langle Ca \rangle_{carb} = \frac{\langle (Ca, Mg)_{0.5} CO_3 \rangle_{riv}}{\left[\frac{u_{CaCO_3}}{u_{Ca}} + \frac{u_{MgCO_3} \langle Mg \rangle_{carb}}{u_{Mg} \langle Ca \rangle_{carb}} \right]} \tag{7}$$

and u_X is the molar mass of component X (Bufe et al., 2021). We estimated $\left[\frac{Na^+}{Ca^{2+}}\right]_{sil}$ based on the assumption that the carbonate content of the bedrock flysch sample with the lowest carbonate content (farthest away from the origin along the regression in $\left[\frac{Na^+}{Ca^{2+}}\right]$-$\left[\frac{Mg^{2+}}{Ca^{2+}}\right]$-space) has a carbonate content of $\langle (Ca, Mg)_{0.5} CO_3 \rangle$=4-10 wt%. The minimum value (4%) is

180 from the lowest observed carbonate content in the field (Chen et al., 2007), whereas the upper bound is chosen so that the

range of values reaches the global endmember value of $\left[\frac{Na^+}{Ca^{2+}}\right]_{sil}$ of 2.86. We then used an average of the resulting $\left[\frac{Na^+}{Ca^{2+}}\right]_{sil}$

estimates with an uncertainty based on half of the range. The corresponding $\left[\frac{Mg^{2+}}{Ca^{2+}}\right]_{sil}$ was then deduced from $\left[\frac{Na^+}{Ca^{2+}}\right]_{sil}$ and

the regression through the bedrock samples (Fig. 3A-B).

We corrected all major elements for atmospheric input using rainwater compositions from the eastern flank of Gongga Shan

185 (Jiang et al., 2018) (Table 1, Table S4). The hotspring endmember is also based on hotspring compositions around Mt

Gongga (Jiang et al., 2018) (Table S5). All hotsprings are very distinct from rock samples, and notably characterized by

$\left[\frac{Na^+}{Ca^{2+}}\right]$-ratios that are 3 – 150-times higher than the highest measured stream water samples (Fig. 3A, Table S5).

Nevertheless, hotspring compositions are highly variable, despite a relatively small area that was sampled (Fig. 3A). In the

inversion, we therefore did not sample the hotspring endmembers from a normal distribution around a mean value. Instead,

190 we picked $[Na^+]_{hs}$, $[Mg^{2+}]_{hs}$, and $[Ca^{2+}]_{hs}$ from uniform distributions that span the interquartile range of all hotspring

samples. Because of a strong correlation between $[Cl^-]_{hs}$ and $[Na^+]_{hs}$ in these hotsprings, we then picked $[Cl^-]_{hs}$ from the

regression between $[Cl^-]_{hs}$ and $[Na^+]_{hs}$. Moreover, we did not consider the hotspring endmember in finding the best-fit

model in the inversion.

As an alternative to the inverse model, we decomposed the data with a common forward approach (Galy and France-Lanord,

195 1999; Moon et al., 2014; Bufe et al., 2021; Jacobson and Blum, 2003; Meybeck, 1987). We assumed that all chloride in the

river water samples was atmospherically derived and use precipitation-averaged $\left[\frac{X}{Cl^-}\right]_{cy}$-ratios of the measured rainwater

(Jiang et al., 2018) (Table S4) to adjust the sample concentrations for rain input. We assumed that our rainwater correction

accounts for possible anthropogenic input of SO_4 from the industrialized Sichuan Basin through acid rain, and we neglected

hotspring contributions. Then, the contributions of silicate and carbonate to the total dissolved Ca^{2+} and Mg^{2+} concentrations

200 were estimated as:

$$[Ca^{2+}]_{sil,fw} = [Na^+]_{spl}\left[\frac{Ca^{2+}}{Na^+}\right]_{sil} \tag{8}$$

$$[Mg^{2+}]_{sil,fw} = [Na^+]_{spl}\left[\frac{Mg^{2+}}{Na^+}\right]_{sil} \tag{9}$$

$$[Ca^{2+}]_{carb,fw} = [Ca^{2+}]_{spl} - [Ca^{2+}]_{sil} \tag{10}$$

$$[Mg^{2+}]_{carb,fw} = [Mg^{2+}]_{spl} - [Mg^{2+}]_{sil} \tag{11}$$

205 **3.3 Cation sums and fractions**

The total sums of cations from silicate and carbonate weathering are:

$$C_{sil} = [Ca^{2+}]_{sil} + [Mg^{2+}]_{sil} + [Na^+] + [K^+] \tag{12}$$

$$C_{carb} = [Ca^{2+}]_{carb} + [Mg^{2+}]_{carb} \tag{13}$$

and in charge equivalents:

$$C_{sil}^{eq} = 2[Ca^{2+}]_{sil} + 2[Mg^{2+}]_{sil} + [Na^+] + [K^+] \tag{14}$$

$$C_{carb}^{eq} = 2[Ca^{2+}]_{carb} + 2[Mg^{2+}]_{carb} \tag{15}$$

The fraction of carbonate weathering is:

$$F_{carb} = \frac{C_{carb}^{eq}}{C_{carb}^{eq} + C_{sil}^{eq}} \tag{16}$$

The fraction of weathering by sulfuric acid (as opposed to carbonic acid) was estimated from sulfate concentrations (Torres et al., 2016; Emberson et al., 2018; Bufe et al., 2021; Galy and France-Lanord, 1999):

$$F_{sulf} = \frac{2[SO_4^{2-}]_w}{2[SO_4^{2-}]_w + [HCO_3^-]} \tag{17}$$

where $[SO_4^{2-}]_w$ is the sulfate concentration that is sourced from sulfide oxidation given by:

$$[SO_4^{2-}]_w = [SO_4^{2-}]_{spl} - [SO_4^{2-}]_{cy} - [SO_4^{2-}]_{hs} \ = [SO_4^{2-}]_{spl} - \alpha_{Ca,cy}\left[\frac{SO_4^{2-}}{Ca^{2+}}\right]_{cy} + \alpha_{Ca,hs}\left[\frac{SO_4^{2-}}{Ca^{2+}}\right]_{hs} \tag{18}$$

Note that this estimate of $[SO_4^{2-}]_w$ assumes that contributions of sulfate from evaporites are negligible in the area, and that any (likely minor) anthropogenic input is captured by the cyclic endmember measured in rainwater samples.

3.4 Estimate of denudation rate

Denudation rates were obtained from existing cosmogenic nuclide concentrations of *in situ*-produced [10]Be (Ouimet et al., 2009; Cook et al., 2018). For two sampled catchments (S18.08 and S18.29) without previous denudation rate estimates, we processed two additional samples for analysis of *in situ* [10]Be following the procedure in Cook et al. (2018). Denudation rates were calculated using CRONUS scripts and the Lal/Stone scaling scheme with a sea-level low latitude nucleogenic production rate of 3.7 (Balco et al., 2008) (Table S6). These denudation rates integrate over the time denuding material resides in the first few upper meters of Earth surface. Although this integration time varies between catchments with different denudation rates, it reflects the timescale of mineral supply to the weathering zone, and is therefore appropriate for comparison to weathering proxies. Where landslides dominate, their stochastic occurrence may disrupt the relationship between soil formation and chemical weathering (Emberson et al., 2016b; Emberson et al., 2016a) and may bias the denudation rate estimates (Niemi et al., 2005; Tofelde et al., 2018; Chen et al., 2020; Yanites et al., 2009). We assume that any such bias is within uncertainty of the denudation rate measurement. Cosmogenic-derived denudation rates incorporate both physical denudation and chemical weathering, but physical denudation rates commonly greatly dominate denudation in

active orogens uplifting siliceous rocks with minor carbonates, such as the ones described here (Erlanger et al., 2021;

235 Gaillardet et al., 1999; Dixon and Von Blanckenburg, 2012; Riebe et al., 2001; West et al., 2005). Thus, we assume that increasing denudation rates correspond to increasing physical erosion rates. Finally, in situ ^{10}Be-derived denudation rates measure the denudation of quartz-containing bedrock. Based on published bedrock descriptions (Jiang et al., 2018; Weller et al., 2013; Chen et al., 2007; Burchfiel et al., 1995) and observations by the authors (Cook et al., 2018), we assume that carbonate and silicate phases in granitoids and metasediments are mixed to a degree that quartz-derived denudation rates

240 approximate the denudation of the entire rock mass. We acknowledge that unquantified uncertainties may arise where significant weathering occurs below the top few meters of the regolith (Riebe and Granger, 2013), or where significant differences in quartz mineral contribution within the bedrock occur, but these uncertainties are unlikely to change the major trends observed in this work.

4 Results

245 In the studied catchments, the concentration of dissolved cations (TDC) generally increases with denudation rates (Fig. 4A). However, the strength of that relationship is greatly influenced by lithology (Fig. 4A). Whereas TDC increases 5 – 10-fold in the Triassic Songpan Ganze flysch, the increase of TDC with denudation in the granitic catchments is less than 2-fold and associated with substantial uncertainty (p=0.19) (Fig. 4A). Mixed flysch – granitic catchments fall in-between the two trends (Fig. 4A). Catchments with Paleozoic metamorphic lithologies have scattered TDC values, many of which fall within the

250 range of values of the Triassic rocks (Fig. 4A). Magnesium and calcium dominate the solute load and constitute 42 – 96% (median 84%) of the TDC. The pattern of increasing TDC is dominated by an increase in calcium concentrations (Fig. 4B), whereas correlations between denudation rate and magnesium, sodium, and potassium concentrations are uncertain (Spearman's p values between 0.1 – 0.8) (Figs. 4C-E). Similarly, no relationship between chloride concentrations and denudation rates is evident (Fig. 4E), but sulfate concentrations show a strong increase with denudation rates in both granites

255 and flysch lithologies (Fig. 4G).

The unmixed cation contributions follow the expectations from the raw data: Cation concentrations from carbonate weathering, C_{carb}, and sulfate from sulfide oxidation, $[SO_4^{2-}]_w$, display a strong relationship with denudation (Fig. 5A, C). In the flysch and in the Paleozoic metamorphics they increase rapidly with denudation rate, whereas the increase in the granitic catchments is weaker, and the mixed catchments are in-between (Fig. 5A, C). In contrast, cations from silicate weathering,

260 precipitation sources, and hotsprings generally show no relationship to denudation rate for any of the lithologies (Fig. 5B, D-E).

The contribution of carbonate weathering to the total solute load from weathering, F_{carb}, strongly increases with denudation irrespective of rock type (Fig. 6A). Even in granitic catchments carbonate weathering contributes more than 50% and up to 94% of the cation charge in most samples (Fig. 6A). Thus, both granites and (meta)sedimentary lithologies have comparable

265 fractions of carbonate weathering (Fig. 6A), even if the absolute concentrations differ (Fig 4). The fraction of weathering by sulfuric acid, F_{sulf}, also increases with increasing denudation rate, although there is a large amount of scatter at higher denudation rates (Fig. 6B). Importantly, F_{sulf} in the weakly metamorphosed flysch catchments appears relatively insensitive to denudation rate, whereas the higher-grade metamorphic catchments have, on average, higher F_{sulf} than the other lithologies. Granitic catchments have widely scattered F_{sulf} values (Fig. 6B).

270 In 16 out of 35 samples (46% of samples), the inferred silicate and/or carbonate cation contributions differ by more than 20% between forward and inverse approaches (Fig. A2). For example, forward-modelled carbonate cation concentrations are more than 20% higher than results from the inversion in 10 samples (29% of samples) and more than 50% higher in 3 samples (9% of samples) (Fig. A2). Silicate cation concentrations inferred from the forward approach are lower in these samples. All of these samples lie outside of the zone formed between the silicate, carbonate, hotspring, and precipitation

275 endmembers which may explain the offset in the results. Conversely, six samples (17%) have more than 20% higher silicate cation concentrations inferred by the forward model (Fig. A2). In all of these samples, the inversion predicts 5 – 40% cation contributions from hotsprings; The hotspring contribution is ignored in the forward approach, and all of the Na^+ is attributed to silicate instead, thereby leading to higher silicate cation contributions. Despite these differences and resulting outliers, the first order trends described in this contribution are unaffected by the choice of unmixing method (Figs. A3, A4).

280 Our concentration measurements cannot be converted into weathering fluxes, because we lack discharge or runoff data for the sampled catchments. However, in comparison to the nearly three-orders-of-magnitude-wide denudation gradient, the mean annual precipitation does not vary widely across the catchments: 82% of the catchments differ by less than a factor of two and 90% by less than a factor of three of precipitation (Table S1). Further, there is no co-variation between precipitation and denudation rate (Fig. 2B, Table S1). Therefore, we assume that the measured concentrations scale with weathering

285 fluxes from these catchments.

5 Discussion

Our analysis indicates that increasing denudation rates lead to an increase in carbonate weathering and sulfide oxidation in all sampled lithologies (Figs. 5-6), likely due to the increased supply of carbonate and sulfide minerals during erosion (Calmels et al., 2007; Torres et al., 2016; Bufe et al., 2021). Conversely, silicate weathering appears to be insensitive to

290 denudation rate and represent a small proportion of the total weathering budget (Figs. 5-6). While the granitic catchments have systematically lower cation concentrations from carbonate weathering than the metasedimentary catchments (Fig. 5A), the fraction of carbonate weathering (F_{carb}) is increasing with denudation and is of similar magnitude in all rock-types (Fig. 6A). Even in catchments underlain by granitoid rocks, weathering of carbonate phases dominates the solute load at denudation rates above 0.1 mm/yr (Fig. 6A). This finding likely arises from the dissolution of trace carbonate minerals

295 disseminated in the crustal granitoids and metapelites that has been described in a number of active mountain ranges (White

et al., 1999; Jacobson et al., 2003; Blum et al., 1998; Emberson et al., 2017; Bufe et al., 2021). In turn, the insensitivity of silicate cation concentrations to denudation (Fig. 5B) is consistent with a kinetic limitation of silicate weathering (West, 2012; West et al., 2005; Gabet and Mudd, 2009). Such kinetic limitation of silicate weathering in conjunction with increasing sulfide oxidation and carbonate weathering across multiple orders of magnitudes of denudation rates (Fig. 5) has

300 recently been documented in the low-grade metasedimentary rocks of southern Taiwan (Bufe et al., 2021). The data presented here suggest that this pattern applies to metasediments in another mountain range, as well as to granitoid rocks. A series of studies on soil formation in metasedimentary and granitic rocks has suggested a link between soil denudation rates and soil production rates, and this sensitivity of soil formation rates to denudation has been used to argue for a relationship between orogenesis and silicate weathering (Riebe et al., 2004; Riebe et al., 2001; Larsen et al., 2014; Dixon et al., 2012;

305 Dixon and Von Blanckenburg, 2012). In contrast, our data confirm that these findings from soil profiles may not directly translate to the catchment scale (West et al., 2005; Dixon and Von Blanckenburg, 2012), due, most likely, to the dissolution of soil waters by fluids from other parts of the landscape – such as landslides (Emberson et al., 2016b). Thus, in active mountain ranges, landscape-scale silicate weathering may be largely insensitive to denudation rates independently of the major lithologies (Bufe et al., 2021; Gabet and Mudd, 2009; West, 2012).

310 Even though yearly average precipitation rates do not vary considerably across the denudation rate gradient, monthly precipitation can vary by a factor of $\sim 5 - 6$ between the high- and low-flow seasons (Jiang et al., 2018). Nevertheless, in small catchments around Mount Gongga, the total dissolved cation concentrations of 80% of rivers is diluted by less than two-fold in the high-flow season (median 1.3-fold) and only Cl^- and Mg^{2+} show substantial dilution (Jiang et al., 2018). Thus, the patterns of concentrations that we described here should broadly mirror the differences in annual weathering fluxes

315 between catchments. Solute concentrations during the high-flow season are expected to carry an elevated proportion of carbonate weathering with respect to the low flow season (Tipper et al., 2006). Thus, by sampling during the low flow season, and by not accounting for cation exchange with suspended sediment from the clay minerals (Tipper et al., 2021), we might overestimate the proportion of silicate weathering (Tipper et al., 2021; Tipper et al., 2006). The dominance of carbonate weathering over silicate weathering in all catchments (Fig. 6) would, therefore, most likely be strengthened with

320 more data across all seasons and/or with suspended sediment data.

The sulfuric-acid-derived sulfate concentrations $[SO_4^{2-}]_w$ and the cation concentrations from silicate weathering allow to estimate the concentration of CO_2 that is sequestered or emitted during chemical weathering (Torres et al., 2016; Emberson et al., 2018). Beyond the calcium carbonate compensation time (~ 10 ky; ref[62]), the moles of CO_2 produced (positive $[CO_2]$) or sequestered (negative $[CO_2]$) during chemical weathering per unit volume of weathering fluid can be expressed as:

325 $$[CO_2] = [SO_4^{2-}]_w^{eq} - 0.5\ C_{carb}^{eq} \qquad (19)$$

(Torres et al., 2016; Bufe et al., 2021) (Fig. 5A) (Table S7). The increase of F_{carb} and F_{sulf} with denudation rate (Fig. 6) leads to a clear change from CO_2 sequestration to CO_2 release (Fig. 7A). These observed trends are most likely explained by the

combination of a supply limitation on coupled pyrite oxidation and carbonate weathering and a limitation of silicate weathering rates by the slow dissolution kinetics of silicate minerals (Bufe et al., 2021; Torres et al., 2016; Calmels et al., 2007; Gabet and Mudd, 2009). Fifteen catchments fall into the long-term CO_2 release field including all of the metamorphic catchments (Paleozoic and Triassic), four of the granitoid catchments, and three mixed granitic/metamorphic catchments (Fig. 7). All of these catchments have denudation rates above 0.19 mm/yr. Compared to the other lithologies, weathering in granitoid catchments remains closest to the CO_2 consumption field across the entire denudation rate gradient (Fig. 7A), largely due to lower sulfate concentrations (Fig. 5C). However, increasing denudation rates, even in granitoid rocks, lead to decreases in the proportion of weathering that contributes to CO_2 drawdown, as sulfate concentrations increase, while silicate cation concentrations are invariable (Figs. 4-6).

Catchments with metamorphosed flysch as well as those with metamorphic Paleozoic sediments (marked by black dots in all data figures) show the highest tendency toward weathering pathways that release CO_2, and they have the highest $\left[SO_4^{2-}\right]_w$ (Fig. 7B). Assuming that sulfide oxidation is limited by the supply of sulfides to the weathering zone (Calmels et al., 2007; Bufe et al., 2021; Torres et al., 2016), we expect a linear increase of sulfate concentrations with denudation (assuming constant runoff). A linear regression of the relationship between sulfate concentration and denudation rate for unmetamorphosed Triassic flysch samples has a gentler slope than a regression through all metapelites, although the scatter in the data leads to overlap in the confidence bands (Fig. 7B). Whereas most of the metamorphic catchments are Paleozoic metapelites, two samples come from metamorphosed Triassic flysch, and they follow the steeper trend of the metamorphic catchments (Fig. 7B). These first data suggest that metamorphism could increase the sulfide content available for oxidation. The production of sulfide by thermal reduction of trace marine sulfates embedded in marine sediments becomes efficient at temperatures above ~500 °C (Goldstein and Aizenshtat, 1994), and could be a viable explanation. The process of metamorphism may therefore alter the balance of weathering pathways and promote CO_2 release once rocks reach the surface, with implications for the evolution of weathering fluxes across the development of an orogen.

6 Conclusion

Water chemistry data from catchments on the eastern margin of the Tibetan plateau that span across three orders of magnitude in denudation rate illustrate the role of lithology in modulating the link between denudation rate and chemical weathering. Perhaps surprisingly, our data show a uniformity in the first-order relationships between weathering and denudation between different lithologies. In particular, in all lithologies, silicate cation concentrations do not increase with increasing denudation rates whereas concentrations of sulfate and of cations from carbonate do show an increase. Whereas granitic and (meta)sedimentary rocks are characterized by similar fractions of carbonate weathering that are increasing with denudation rate, the (meta)sediments have higher absolute concentrations of sulfate and of cations from carbonate weathering, likely due to higher concentrations of these minor phases in the bedrock. In combination, the weathering

reactions lead to a transition from CO_2 drawdown to CO_2 release at denudation rates >0.2 mm/yr, even in granitic

360 catchments. Our data also suggest, albeit with large uncertainties, that the contribution of sulfuric acid to weathering from a given lithology can be increased due to metamorphism of that rock type. Consequently, as mountain belts mature and denudation exposes more deeply buried rocks, weathering pathways may increasingly trend towards CO_2 release at high denudation rates.
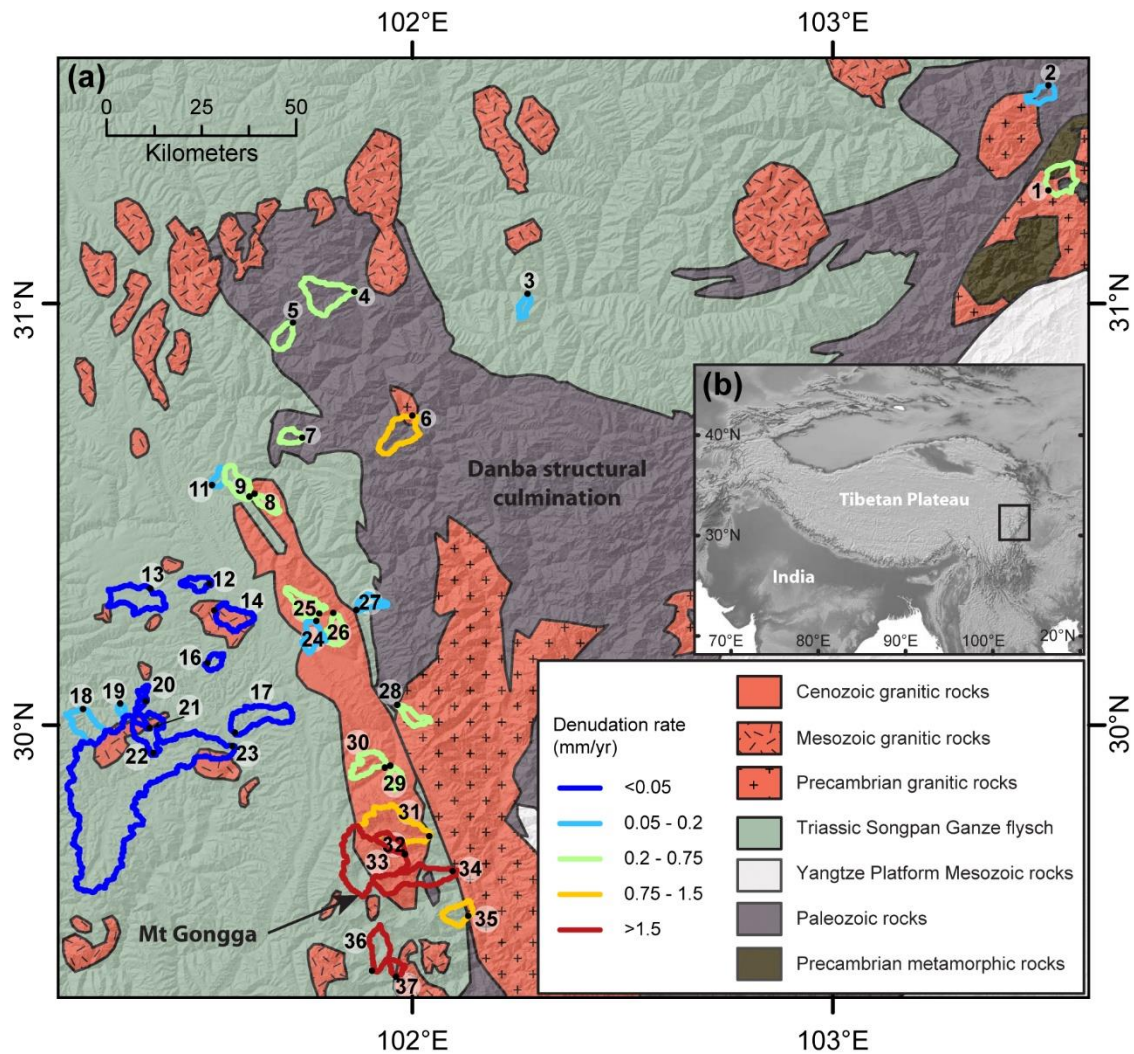
Figures

Figure 1: Overview of the study area

(a) Simplified geologic map of the study area showing sample locations, sample numbers, and catchment outlines. Outline color indicates
[10]Be basin-wide denudation rate from Cook et al. (2018), with two samples from this study (Table S6). (b) Location of study area.

Earth **Surface**
Dynamics
Discussions
EGU
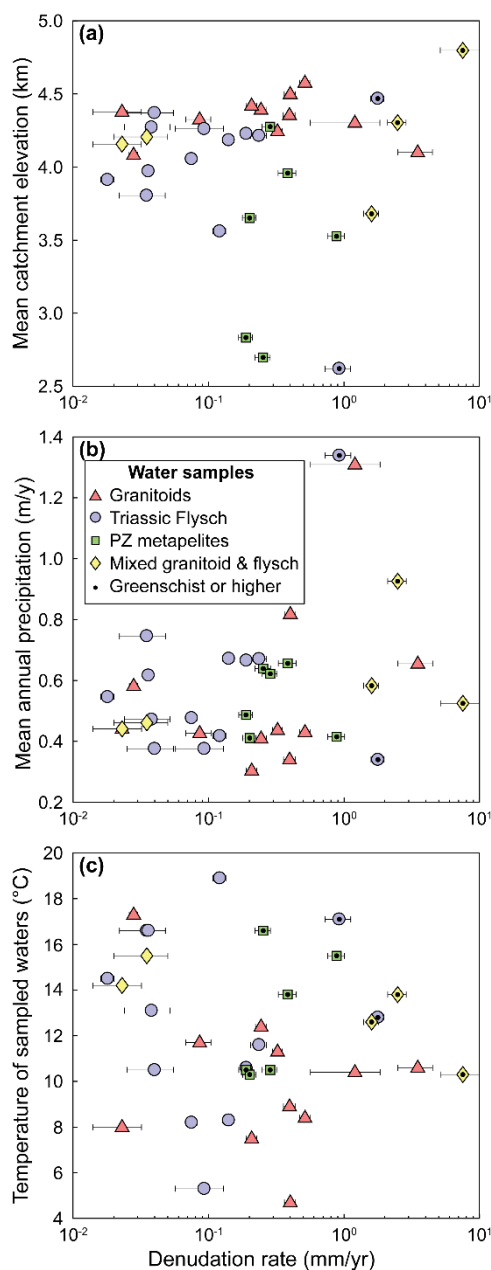
Figure 2: Variability of topographic and climatic parameter across the denudation gradient

(a) Catchment-averaged elevation upstream of each sample as a function of denudation rate. (b) TRMM-derived mean annual precipitation
375   in the catchment as a function of denudation rate. (c) Temperature of sampled waters as a function of denudation rate. Catchments
underlain by different lithologies are distinguished by symbols and color. Datapoints with a black dot are metamorphosed to greenschist
facies or higher.

Earth **Surface**
Dynamics
Discussions
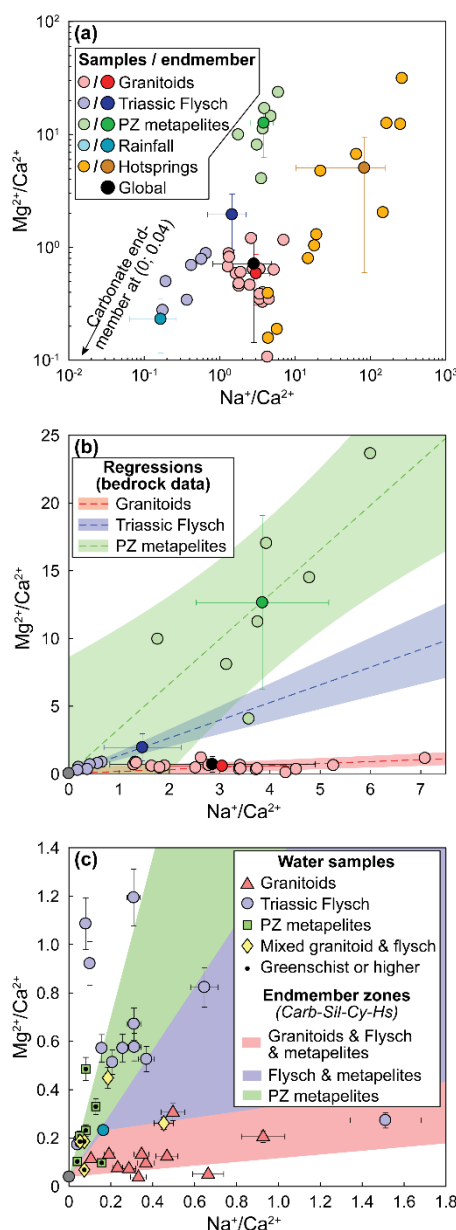
380 **Figure 3: Endmembers and mixing lines in Na⁺/Ca²⁺ – Mg²⁺/Ca²⁺ space**

(a) Small points mark individual bedrock, rain water, and hotspring chemistry (Table S3) (Jiang et al., 2018; Chen et al., 2007; Weller et al., 2013). Large points mark corresponding endmember estimates (Table 1). Silicate endmembers for granitoids and Paleozoic metamorphics as well as for the rainfall endmember are estimated from a mean and standard deviation of individual datapoints. The flysch silicate endmember was derived from a regression through the bedrock data and estimates of the carbonate content in the bedrock flysch

385 samples (see text). For hotsprings, the endmember is the median and interquartile range. The carbonate endmember cannot be shown in logarithmic space (b) Bedrock chemistry and endmembers with mixing lines between silicate and carbonate endmembers. (c) Individual water samples within the endmember space. Colored areas mark the space between the carbonate, silicate, precipitation, and hotspring

endmembers for each lithology. Note that spaces are overlapping. Catchments underlain by different lithologies are distinguished by symbols and color. Datapoints with a black dot are metamorphosed to greenschist facies or higher.

390
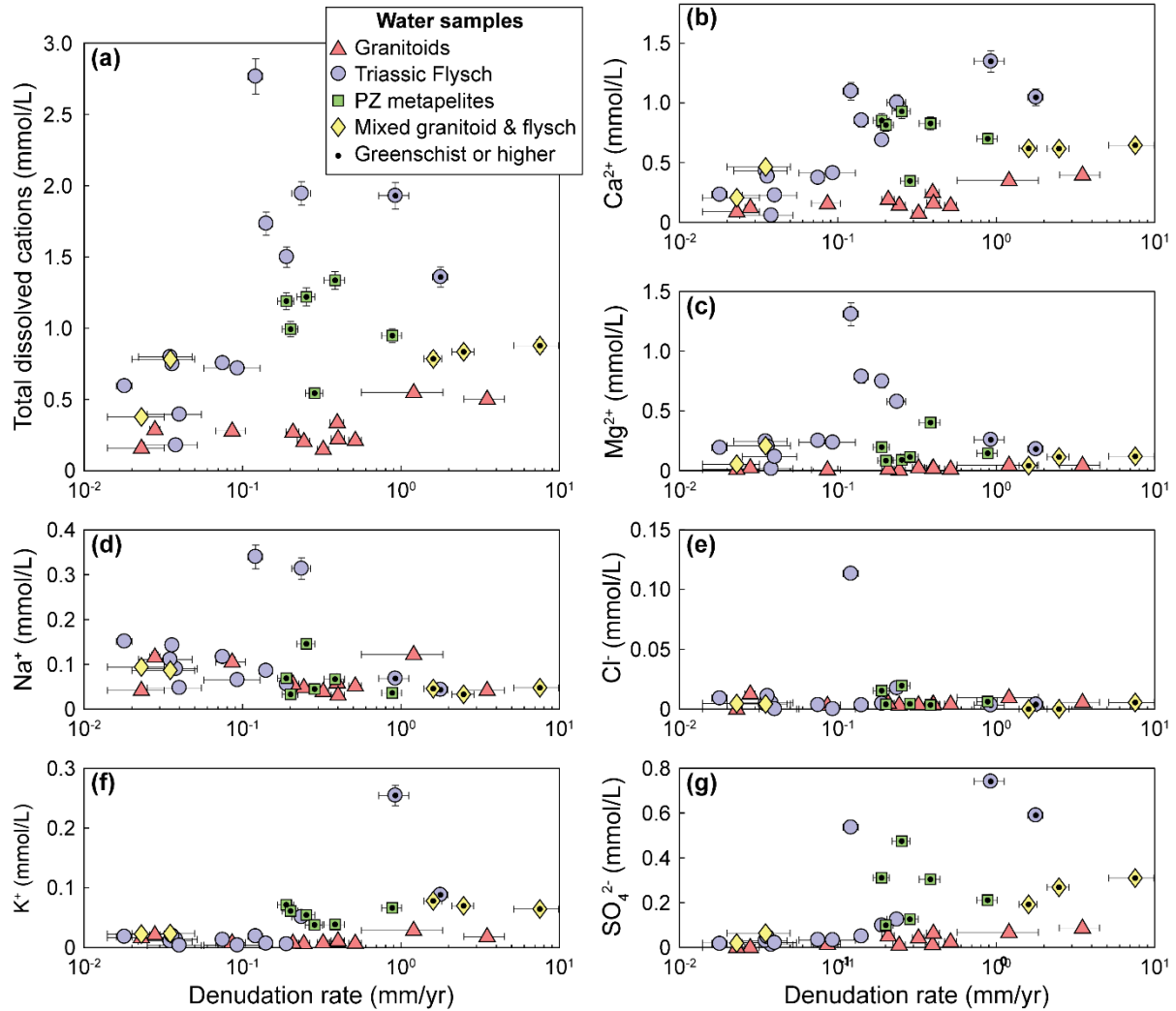
Figure 4: Solute concentrations vs. denudation rate

(a) Total dissolved cations. Spearman's rank correlation coefficient and associated p-value: $rho_{granite}^{TDS} = 0.43$, $p_{granite}^{TDS} = 0.19$;

$rho_{flysch}^{TDC} = 0.69$, $p_{flysch}^{TDC} = 0.01$. (B) Ca^{2+} concentrations $rho_{granite}^{Ca^{2+}} = 0.62$, $p_{granite}^{Ca^{2+}} = 0.04$; $rho_{flysch}^{Ca^{2+}} = 0.77$, $p_{flysch}^{Ca^{2+}} = 0.003$. (C)

395 Mg^{2+} concentrations. (D) Na^+ concentrations. (E) K^+ concentrations. (F) Cl^- concentrations. (G) SO_4^{2-} concentrations $rho_{granite}^{SO_4^{2-}} = 0.82$,

$p_{granite}^{SO_4^{2-}} = 0.002$; $rho_{flysch}^{SO_4^{2-}} = 0.93$, $p_{flysch}^{SO_4^{2-}} < 0.002$. Catchments underlain by different lithologies are distinguished by symbols and color. Datapoints with a black dot are metamorphosed to greenschist facies or higher.
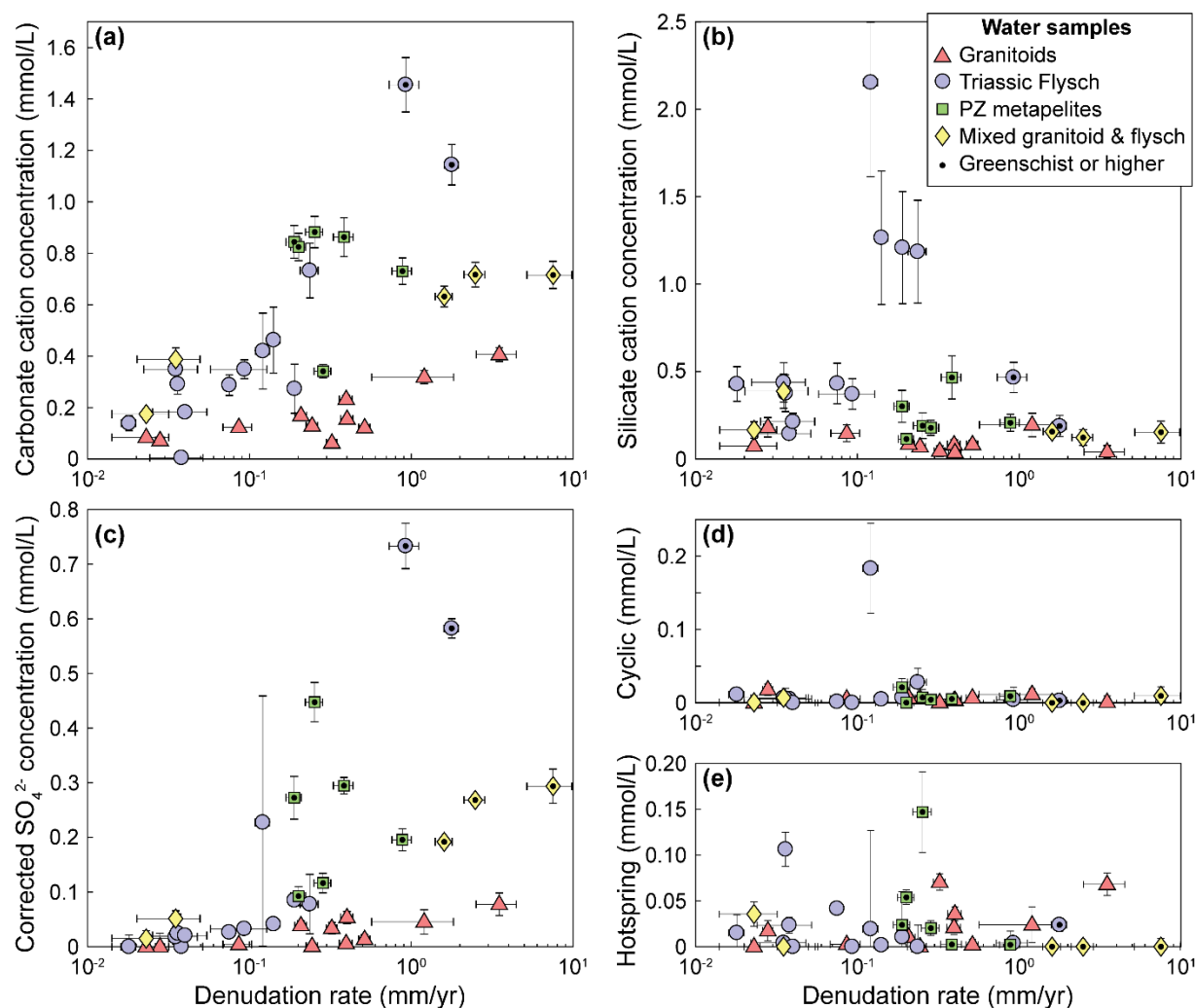
Figure 5: Unmixed contributions to the solute load

(a) Cation concentrations from carbonate weathering. (b) Cation concentrations from silicate weathering. (c) Sulfate concentrations corrected for precipitation and inferred to derive from sulfide oxidation. (d) Cation concentrations from precipitation sources. (e) Cation concentrations from hotspring sources. Catchments underlain by different lithologies are distinguished by symbols and color. Datapoints with a black dot are metamorphosed to greenschist facies or higher.
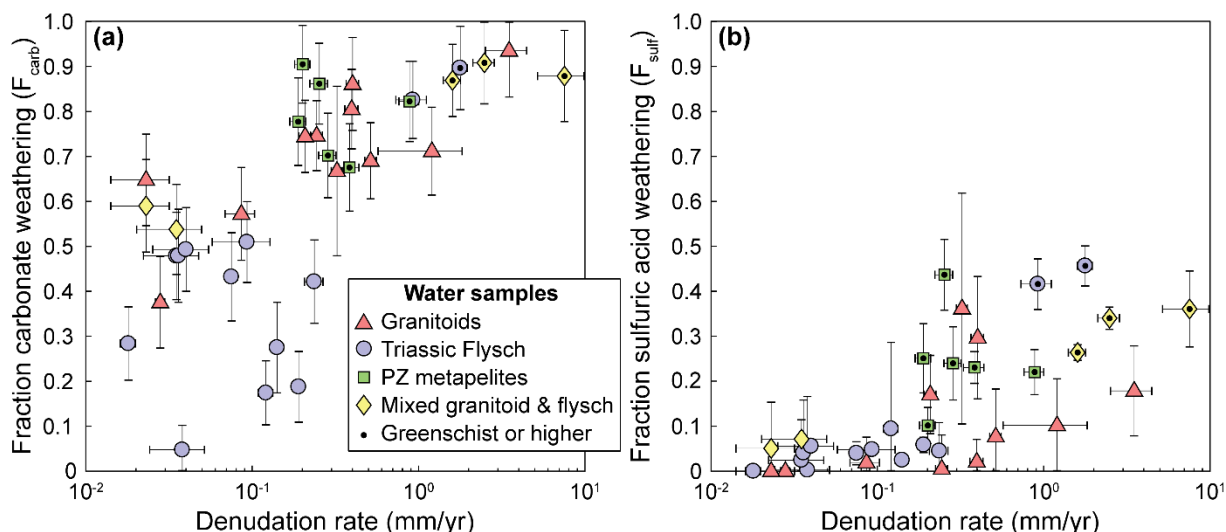
Figure 6: Fraction of carbonate weathering and weathering by sulfuric acid

(a) Fraction of carbonate weathering (eq. 16). (b) Fraction of weathering by sulfuric acid (eq. 17). Symbols indicate catchment lithology. Catchments underlain by different lithologies are distinguished by symbols and color. Datapoints with a black dot are metamorphosed to greenschist facies or higher.
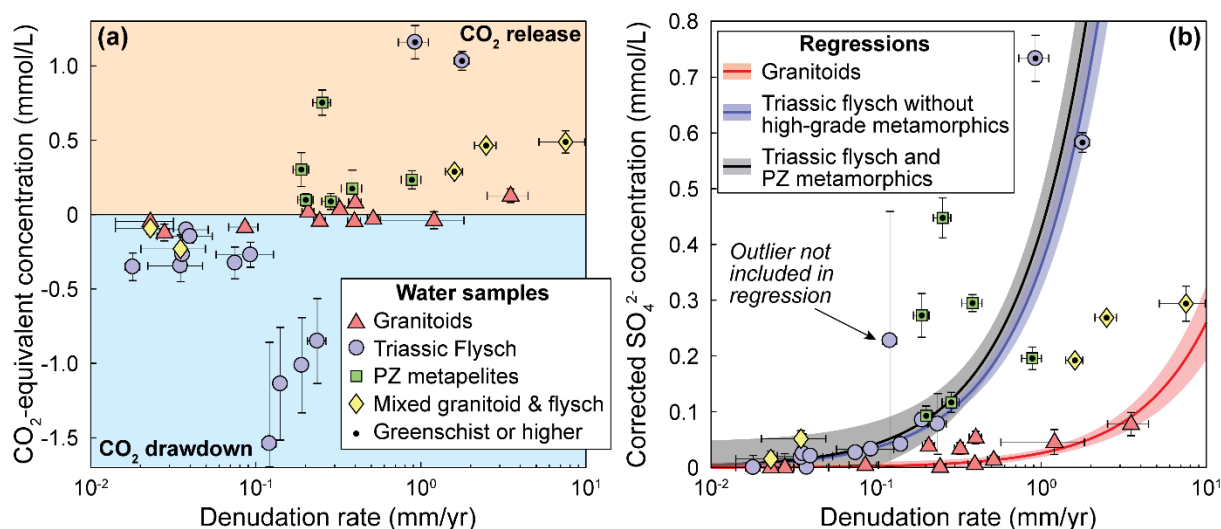
Figure 7: Influence of weathering on carbon cycle

(a) Equivalent concentration of CO_2 released or consumed. (b) Sulfate from sulfide oxidation with linear regressions (curved due to semi-log plot). Blue regression is through only the unmetamorphosed flysch. Black regression is through all of the Triassic flysch and Paleozoic metamorphic rocks. Symbols indicate catchment lithology. Catchments underlain by different lithologies are distinguished by symbols and color. Datapoints with a black dot are metamorphosed to greenschist facies or higher.

Table 1. Input endmembers for mixing model

Endmember	Na/Ca	± Na/Ca	Mg/Ca	± Mg/Ca	Cl/Ca	± Cl/Ca
Silicate: Granite	2.78	1.53	0.59	0.28	0	0
Silicate: Paleozoic metapelites	3.76	1.32	11.24	6.42	0	0
Silicate: Flysch	1.46	0.77	1.95	1.00	0	0
Silicate: Global	2.86	2.04	0.71	0.57	0	0
Carbonate	0	0	0.04	0.13	0	0
Precipitation	0.16	0.12	0.23	0.11	0.98	0.47

Appendix A: Supporting figures

420
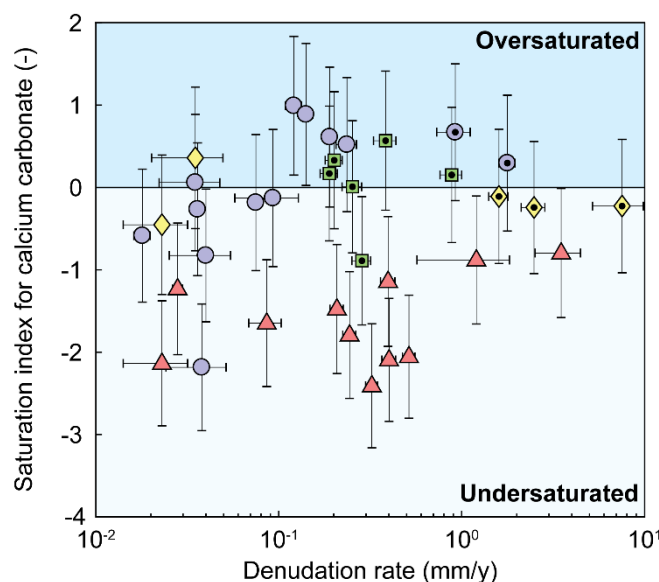
Figure A1: Saturation index of samples with respect to calcium carbonate

Catchments underlain by different lithologies are distinguished by symbols and color. Datapoints with a black dot are metamorphosed to greenschist facies or higher.

425
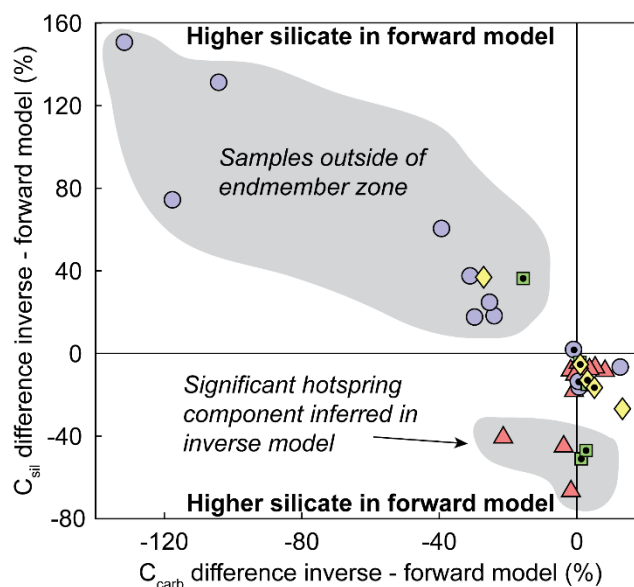
Figure A2: Difference between forward and inverse unmixing approaches

Positive values indicate that the inverse approach predicts higher cation ratios than the forward approach. All samples in the upper left quadrant are outside of the carbonate – silicate – hotspring – precipitation endmember space in Na^+/Ca^{2+} – Mg^{2+}/Ca^{2+} space (Fig. 3C). The

five samples with lower inverse silicate cation concentrations are characterized by >5% hotspring contribution that is not accounted for in

430   the forward model (see text). Catchments underlain by different lithologies are distinguished by symbols and color. Datapoints with a

black dot are metamorphosed to greenschist facies or higher.
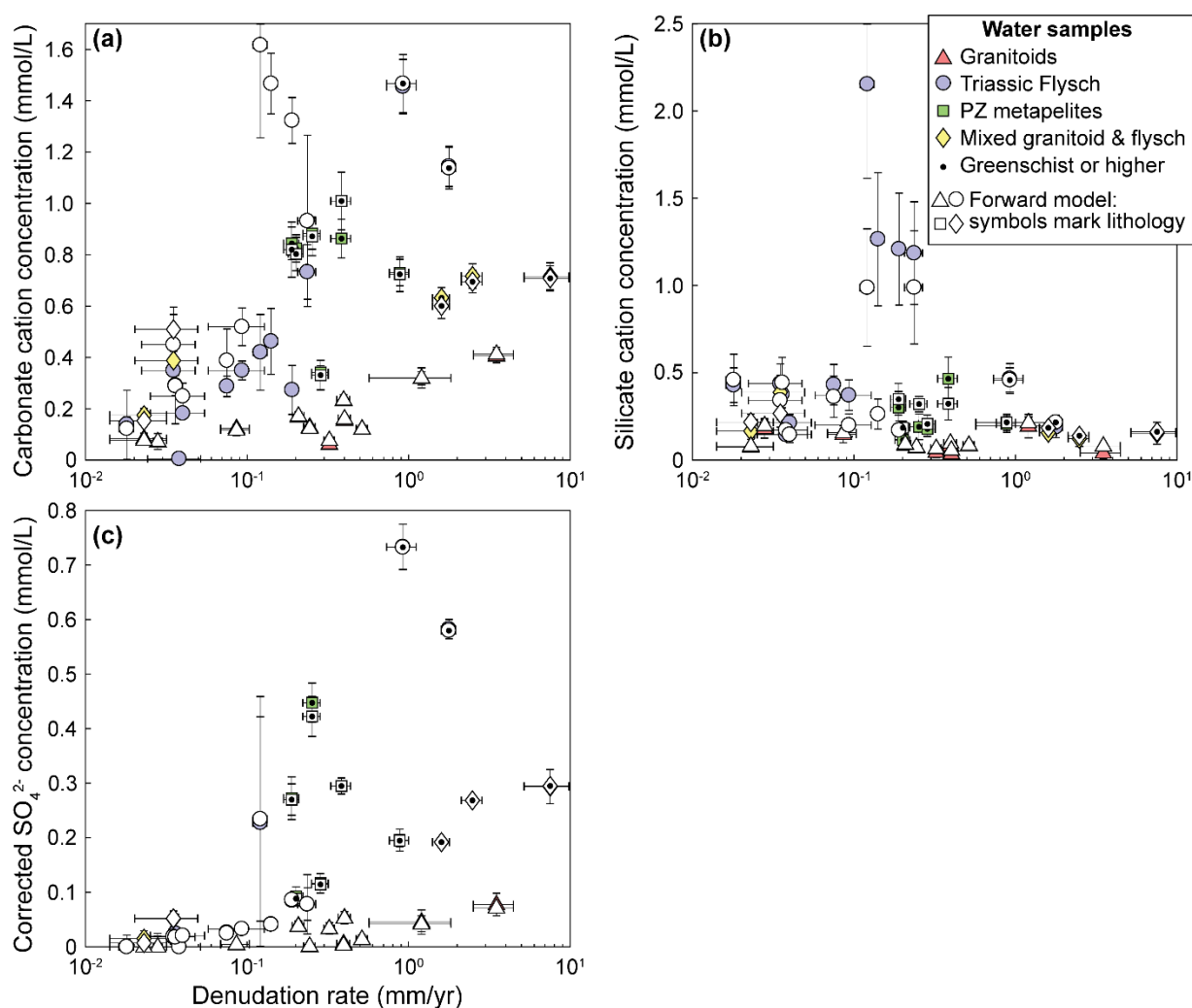
Figure A3: Forward model results for silicate, carbonate, and sulfide weathering contributions

435   Data from Figure 5 plotted with results from the forward model (white points). Lithology in the data from the forward model is

distinguished by symbology only. Where results from forward and inverse approaches are similar, symbols overlap.
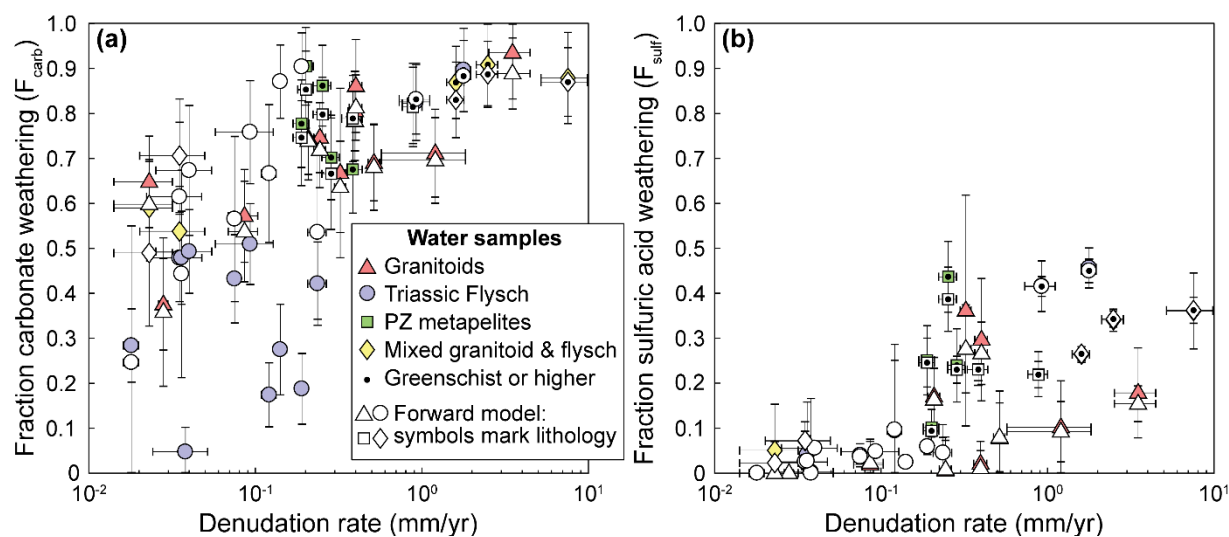
Figure A4: Forward model results for the fraction of carbonate weathering and weathering by sulfuric acid

Data from Figure 6 plotted with results from the forward model (white points). Lithology in the data from the forward model is
440   distinguished by symbology only. Where results from forward and inverse approaches are similar, symbols overlap.

Data Availability

All data used in this paper are included as tables in the Supplement.

Author contribution

K.L.C. and N.H. conceived the study and collected samples in the field. A.B., H.W., and A.G. contributed to laboratory
445 analyses. K.L.C. and A.B. led the data analysis and interpretation and wrote the manuscript with input from all authors.

Competing interest

The authors declare that they have no conflict of interest.

Acknowledgements

We thank Fan Xuanmei and Chen Jie for help with fieldwork logistics. Bernhard Zimmermann, Jutta Schlegel, Daniel Frick,
450 Andrea Gottsche, Tanya Goldberg, and the HELGES Lab are thanked for laboratory assistance.

Financial support

AB has received funding from the European Union's Horizon 2020 research and innovation
programme under the Marie Sklodowska-Curie grant agreement No 841663.

References

Anderson, S. P., Drever, J. I., Frost, C. D., and Holden, P.: Chemical weathering in the foreland of a retreating glacier, Geochim. Cosmochim. Ac., 64, 1173-1189, https://doi.org/10.1016/S0016-7037(99)00358-0, 2000.

Balco, G., Stone, J. O., Lifton, N. A., and Dunai, T. J.: A complete and easily accessible means of calculating surface exposure ages or erosion rates from 10Be and 26Al measurements, Quat. Geochronol., 3, 174-195, http://dx.doi.org/10.1016/j.quageo.2007.12.001, 2008.

Berner, R. A., Lasaga, A. C., and Garrels, R. M.: The carbonate-silicate geochemical cycle and its effect on atmospheric carbon dioxide over the past 100 million years, Am. J. Sci., 283, 641-683, 10.2475/ajs.283.7.641, 1983.

Blattmann, T. M., Wang, S. L., Lupker, M., Märki, L., Haghipour, N., Wacker, L., Chung, L. H., Bernasconi, S. M., Plötze, M., and Eglinton, T. I.: Sulphuric acid-mediated weathering on Taiwan buffers geological atmospheric carbon sinks, Sci. Rep., 9, 2945, 10.1038/s41598-019-39272-5, 2019.

Blum, J. D., Gazis, C. A., Jacobson, A. D., and Page Chamberlain, C.: Carbonate versus silicate weathering in the Raikhot watershed within the High Himalayan Crystalline Series, Geology, 26, 411-414, 10.1130/0091-7613(1998)026<0411:CVSWIT>2.3.CO;2, 1998.

Bookhagen, B. and Burbank, D. W.: Toward a complete Himalayan hydrological budget: Spatiotemporal distribution of snowmelt and rainfall and their impact on river discharge, J. Geophys. Res., 115, F03019, 10.1029/2009JF001426, 2010.

Bufe, A., Hovius, N., Emberson, R., Rugenstein, J. K. C., Galy, A., Hassenruck-Gudipati, H. J., and Chang, J.-M.: Co-variation of silicate, carbonate and sulfide weathering drives CO2 release with erosion, Nat. Geosci., 14, 211-216, 10.1038/s41561-021-00714-3, 2021.

Burchfiel, B. C., Zhiliang, C., Yupinc, L., and Royden, L. H.: Tectonics of the Longmen Shan and Adjacent Regions, Central China, International Geology Review, 37, 661-735, 10.1080/00206819509465424, 1995.

Burke, A., Present, T. M., Paris, G., Rae, E. C. M., Sandilands, B. H., Gaillardet, J., Peucker-Ehrenbrink, B., Fischer, W. W., McClelland, J. W., Spencer, R. G. M., Voss, B. M., and Adkins, J. F.: Sulfur isotopes in rivers: Insights into global weathering budgets, pyrite oxidation, and the modern sulfur cycle, Earth Planet. Sc. Lett., 496, 168-177, https://doi.org/10.1016/j.epsl.2018.05.022, 2018.

Calmels, D., Gaillardet, J., Brenot, A., and France-Lanord, C.: Sustained sulfide oxidation by physical erosion processes in the Mackenzie River basin: Climatic perspectives, Geology, 35, 1003-1006, 10.1130/g24132a.1, 2007.

Caves Rugenstein, J. K., Ibarra, D. E., and von Blanckenburg, F.: Neogene cooling driven by land surface reactivity rather than increased weathering fluxes, Nature, 571, 99-102, 10.1038/s41586-019-1332-y, 2019.

Chen, C.-Y., Willett, S. D., West, A. J., Dadson, S., Hovius, N., Christl, M., and Shyu, J. B. H.: The impact of storm-triggered landslides on sediment dynamics and catchment-wide denudation rates in the southern Central Range of Taiwan following the extreme rainfall event of Typhoon Morakot, Earth Surf. Proc. Land., 45, 548-564, 10.1002/esp.4753, 2020.

Chen, Y., Liu, F., Zhang, H., Nie, L., and Jiang, L.: Elemental and Sm-Nd isotopic geochemistry on detrital sedimentary rocks in the Ganzi-Songpan block and Longmen Mountains, Frontiers of Earth Science in China, 1, 60, 2007.

Cook, K. L., Hovius, N., Wittmann, H., Heimsath, A. M., and Lee, Y.-H.: Causes of rapid uplift and exceptional topography of Gongga Shan on the eastern margin of the Tibetan Plateau, Earth Planet. Sc. Lett., 481, 328-337, https://doi.org/10.1016/j.epsl.2017.10.043, 2018.

Das, A., Chung, C.-H., and You, C.-F.: Disproportionately high rates of sulfide oxidation from mountainous river basins of Taiwan orogeny: Sulfur isotope evidence, Geophys. Res. Lett., 39, L12404, 10.1029/2012GL051549, 2012.

Dessert, C., Dupré, B., Gaillardet, J., François, L. M., and Allègre, C. J.: Basalt weathering laws and the impact of basalt weathering on the global carbon cycle, Chem. Geol., 202, 257-273, https://doi.org/10.1016/j.chemgeo.2002.10.001, 2003.

Dixon, J. L. and von Blanckenburg, F.: Soils as pacemakers and limiters of global silicate weathering, CR. Geosci., 344, 597-609, http://dx.doi.org/10.1016/j.crte.2012.10.012, 2012.

Dixon, J. L., Chadwick, O. A., and Vitousek, P. M.: Climate-driven thresholds for chemical weathering in postglacial soils of New Zealand, J. Geophys. Res., 121, 1619-1634, 10.1002/2016JF003864, 2016.

Dixon, J. L., Hartshorn, A. S., Heimsath, A. M., DiBiase, R. A., and Whipple, K. X.: Chemical weathering response to tectonic forcing: A soils perspective from the San Gabriel Mountains, California, Earth Planet. Sc. Lett., 323–324, 40-49, http://dx.doi.org/10.1016/j.epsl.2012.01.010, 2012.

Drever, J. I. and Clow, D. W.: Weathering Rates in Catchments, in: Chemical Weathering Rates of Silicate Minerals, edited by: White, A. F., and Brantley, S. L., De Gruyter, 463-484, doi:10.1515/9781501509650-012, 2018.

Drever, J. I. and Zobrist, J.: Chemical weathering of silicate rocks as a function of elevation in the southern Swiss Alps, Geochim. Cosmochim. Ac., 56, 3209-3216, https://doi.org/10.1016/0016-7037(92)90298-W, 1992.

Emberson, R., Galy, A., and Hovius, N.: Combined effect of carbonate and biotite dissolution in landslides biases silicate weathering proxies, Geochim. Cosmochim. Ac., 213, 418-434, http://dx.doi.org/10.1016/j.gca.2017.07.014, 2017.

Emberson, R., Galy, A., and Hovius, N.: Weathering of Reactive Mineral Phases in Landslides Acts as a Source of Carbon Dioxide in Mountain Belts, J. Geophys. Res., 123, 2695-2713, doi:10.1029/2018JF004672, 2018.

Emberson, R., Hovius, N., Galy, A., and Marc, O.: Oxidation of sulfides and rapid weathering in recent landslides, Earth Surf. Dynam., 4, 727-742, 10.5194/esurf-4-727-2016, 2016a.

Emberson, R., Hovius, N., Galy, A., and Marc, O.: Chemical weathering in active mountain belts controlled by stochastic bedrock landsliding, Nat. Geosci., 9, 42-45, 10.1038/ngeo2600, 2016b.

510 Erlanger, E. D., Rugenstein, J. K. C., Bufe, A., Picotti, V., and Willett, S. D.: Controls on Physical and Chemical Denudation in a Mixed Carbonate-Siliciclastic Orogen, J. Geophys. Res., n/a, e2021JF006064, https://doi.org/10.1029/2021JF006064, 2021.

Gabet, E. J. and Mudd, S. M.: A theoretical model coupling chemical weathering rates with denudation rates, Geology, 37, 151-154, 10.1130/g25270a.1, 2009.

Gaillardet, J., Dupré, B., Louvat, P., and Allègre, C. J.: Global silicate weathering and CO2 consumption rates deduced from the chemistry
515 of large rivers, Chem. Geol., 159, 3-30, http://dx.doi.org/10.1016/S0009-2541(99)00031-5, 1999.

Gaillardet, J., Calmels, D., Romero-Mujalli, G., Zakharova, E., and Hartmann, J.: Global climate control on carbonate weathering intensity, Chem. Geol., https://doi.org/10.1016/j.chemgeo.2018.05.009, 2018.

Galy, A. and France-Lanord, C.: Weathering processes in the Ganges–Brahmaputra basin and the riverine alkalinity budget, Chem. Geol., 159, 31-60, http://dx.doi.org/10.1016/S0009-2541(99)00033-9, 1999.

520 Godsey, S. E., Hartmann, J., and Kirchner, J. W.: Catchment chemostasis revisited: Water quality responds differently to variations in weather and climate, Hydrol. Process., 33, 3056-3069, 10.1002/hyp.13554, 2019.

Goldstein, T. and Aizenshtat, Z.: Thermochemical sulfate reduction a review, Journal of Thermal Analysis and Calorimetry, 42, 241-290, 10.1007/bf02547004, 1994.

Guo, J., Ma, L., Gaillardet, J., Sak, P. B., Pereyra, Y., and Engel, J.: Reconciling chemical weathering rates across scales: Application of
525 uranium-series isotope systematics in volcanic weathering clasts from Basse-Terre Island (French Guadeloupe), Earth Planet. Sc. Lett., 115874, https://doi.org/10.1016/j.epsl.2019.115874, 2019.

Hartmann, J., Jansen, N., Dürr, H. H., Kempe, S., and Köhler, P.: Global CO2-consumption by chemical weathering: What is the contribution of highly active weathering regions?, Global Planet. Change, 69, 185-194, https://doi.org/10.1016/j.gloplacha.2009.07.007, 2009.

530 Hilley, G. E., Chamberlain, C. P., Moon, S., Porder, S., and Willett, S. D.: Competition between erosion and reaction kinetics in controlling silicate-weathering rates, Earth Planet. Sc. Lett., 293, 191-199, http://dx.doi.org/10.1016/j.epsl.2010.01.008, 2010.

Hilton, R. G. and West, A. J.: Mountains, erosion and the carbon cycle, Nat. Rev. Earth Environ., 1, 284-299, 10.1038/s43017-020-0058-6, 2020.

Huang, M. H., Buick, I. S., and Hou, L. W.: Tectonometamorphic Evolution of the Eastern Tibet Plateau: Evidence from the Central
535 Songpan–Garzê Orogenic Belt, Western China, Journal of Petrology, 44, 255-278, 10.1093/petrology/44.2.255, 2003.

Ibarra, D. E., Caves, J. K., Moon, S., Thomas, D. L., Hartmann, J., Chamberlain, C. P., and Maher, K.: Differential weathering of basaltic and granitic catchments from concentration–discharge relationships, Geochim. Cosmochim. Ac., 190, 265-293, https://doi.org/10.1016/j.gca.2016.07.006, 2016.

Jacobson, A. D. and Blum, J. D.: Relationship between mechanical erosion and atmospheric CO2 consumption in the New Zealand
540 Southern Alps, Geology, 31, 865-868, 10.1130/g19662.1, 2003.

Jacobson, A. D., Blum, J. D., Chamberlain, C. P., Craw, D., and Koons, P. O.: Climatic and tectonic controls on chemical weathering in the New Zealand Southern Alps, Geochim. Cosmochim. Ac., 67, 29-46, http://dx.doi.org/10.1016/S0016-7037(02)01053-0, 2003.

Jiang, H., Liu, W., Xu, Z., Zhou, X., Zheng, Z., Zhao, T., Zhou, L., Zhang, X., Xu, Y., and Liu, T.: Chemical weathering of small catchments on the Southeastern Tibetan Plateau I: Water sources, solute sources and weathering rates, Chem. Geol., 500, 159-174,
545 https://doi.org/10.1016/j.chemgeo.2018.09.030, 2018.

Kump, L. R. and Arthur, M. A.: Global Chemical Erosion during the Cenozoic: Weatherability Balances the Budgets, in: Tectonic Uplift and Climate Change, edited by: Ruddiman, W. F., Springer US, Boston, MA, 399-426, 10.1007/978-1-4615-5935-1_18, 1997.

Larsen, I. J., Almond, P. C., Eger, A., Stone, J. O., Montgomery, D. R., and Malcolm, B.: Rapid Soil Production and Weathering in the Southern Alps, New Zealand, Science, 343, 637-640, 10.1126/science.1244908, 2014.

550 Lasaga, A. C.: Chemical kinetics of water-rock interactions, J. Geophys. Res., 89, 4009-4025, 10.1029/JB089iB06p04009, 1984.

Li, G., Hartmann, J., Derry, L. A., West, A. J., You, C.-F., Long, X., Zhan, T., Li, L., Li, G., Qiu, W., Li, T., Liu, L., Chen, Y., Ji, J., Zhao, L., and Chen, J.: Temperature dependence of basalt weathering, Earth Planet. Sc. Lett., 443, 59-69, https://doi.org/10.1016/j.epsl.2016.03.015, 2016.

Märki, L., Lupker, M., France-Lanord, C., Lavé, J., Gallen, S., Gajurel, A. P., Haghipour, N., Leuenberger-West, F., and Eglinton, T.: An
555 unshakable carbon budget for the Himalaya, Nat. Geosci., 10.1038/s41561-021-00815-z, 2021.

Meybeck, M.: Global chemical weathering of surficial rocks estimated from river dissolved loads, Am. J. Sci., 287, 401-428, 10.2475/ajs.287.5.401, 1987.

Moon, S., Chamberlain, C. P., and Hilley, G. E.: New estimates of silicate weathering rates and their uncertainties in global rivers, Geochim. Cosmochim. Ac., 134, 257-274, http://dx.doi.org/10.1016/j.gca.2014.02.033, 2014.

560 Morse, J. W. and Arvidson, R. S.: The dissolution kinetics of major sedimentary carbonate minerals, Earth Sci. Rev., 58, 51-84, http://dx.doi.org/10.1016/S0012-8252(01)00083-6, 2002.

Niemi, N. A., Oskin, M., Burbank, D. W., Heimsath, A. M., and Gabet, E. J.: Effects of bedrock landslides on cosmogenically determined erosion rates, Earth Planet. Sc. Lett., 237, 480-498, http://dx.doi.org/10.1016/j.epsl.2005.07.009, 2005.

Oeser, R. A. and von Blanckenburg, F.: Do degree and rate of silicate weathering depend on plant productivity?, Biogeosciences, 17,
565 4883-4917, 10.5194/bg-17-4883-2020, 2020.

Ouimet, W. B., Whipple, K. X., and Granger, D. E.: Beyond threshold hillslopes: Channel adjustment to base-level fall in tectonically active mountain ranges, Geology, 37, 579-582, 10.1130/g30013a.1, 2009.

Raymo, M. E. and Ruddiman, W. F.: Tectonic forcing of late Cenozoic climate, Nature, 359, 117-122, 10.1038/359117a0, 1992.

570   Riebe, C. S. and Granger, D. E.: Quantifying effects of deep and near-surface chemical erosion on cosmogenic nuclides in soils, saprolite, and sediment, Earth Surf. Proc. Land., 38, 523-533, https://doi.org/10.1002/esp.3339, 2013.

Riebe, C. S., Kirchner, J. W., and Finkel, R. C.: Erosional and climatic effects on long-term chemical weathering rates in granitic landscapes spanning diverse climate regimes, Earth Planet. Sc. Lett., 224, 547-562, http://dx.doi.org/10.1016/j.epsl.2004.05.019, 2004.

Riebe, C. S., Kirchner, J. W., Granger, D. E., and Finkel, R. C.: Strong tectonic and weak climatic control of long-term chemical weathering rates, Geology, 29, 511-514, 10.1130/0091-7613(2001)029<0511:stawcc>2.0.co;2, 2001.

575   Roger, F., Jolivet, M., and Malavieille, J.: The tectonic evolution of the Songpan-Garzê (North Tibet) and adjacent areas from Proterozoic to Present: A synthesis, J. Asian Earth Sci., 39, 254-269, https://doi.org/10.1016/j.jseaes.2010.03.008, 2010.

Roger, F., Malavieille, J., Leloup, P. H., Calassou, S., and Xu, Z.: Timing of granite emplacement and cooling in the Songpan–Garzê Fold Belt (eastern Tibetan Plateau) with tectonic implications, J. Asian Earth Sci., 22, 465-481, https://doi.org/10.1016/S1367-9120(03)00089-0, 2004.

580   Searle, M. P., Roberts, N. M. W., Chung, S.-L., Lee, Y.-H., Cook, K. L., Elliott, J. R., Weller, O. M., St-Onge, M. R., Xu, X.-W., Tan, X.-B., and Li, K.: Age and anatomy of the Gongga Shan batholith, eastern Tibetan Plateau, and its relationship to the active Xianshui-he fault, Geosphere, 12, 948-970, 10.1130/GES01244.1, 2016.

Tipper, E. T., Bickle, M. J., Galy, A., West, A. J., Pomiès, C., and Chapman, H. J.: The short term climatic sensitivity of carbonate and silicate weathering fluxes: Insight from seasonal variations in river chemistry, Geochim. Cosmochim. Ac., 70, 2737-2754,

585   https://doi.org/10.1016/j.gca.2006.03.005, 2006.

Tipper, E. T., Stevenson, E. I., Alcock, V., Knight, A. C. G., Baronas, J. J., Hilton, R. G., Bickle, M. J., Larkin, C. S., Feng, L., Relph, K. E., and Hughes, G.: Global silicate weathering flux overestimated because of sediment–water cation exchange, Proc. Natl. Acad. Sci. U.S.A., 118, e2016430118, 10.1073/pnas.2016430118, 2021.

Tofelde, S., Duesing, W., Schildgen, T. F., Wickert, A. D., Wittmann, H., Alonso, R. N., and Strecker, M.: Effects of deep-seated versus 590 shallow hillslope processes on cosmogenic 10Be concentrations in fluvial sand and gravel, Earth Surf. Proc. Land., 43, 3086-3098, doi:10.1002/esp.4471, 2018.

Torres, M. A., West, A. J., and Li, G.: Sulphide oxidation and carbonate dissolution as a source of CO2 over geological timescales, Nature, 507, 346-349, 10.1038/nature13030, 2014.

Torres, M. A., West, A. J., Clark, K. E., Paris, G., Bouchez, J., Ponton, C., Feakins, S. J., Galy, V., and Adkins, J. F.: The acid and 595 alkalinity budgets of weathering in the Andes–Amazon system: Insights into the erosional control of global biogeochemical cycles, Earth Planet. Sc. Lett., 450, 381-391, http://dx.doi.org/10.1016/j.epsl.2016.06.012, 2016.

Uhlig, D. and von Blanckenburg, F.: How Slow Rock Weathering Balances Nutrient Loss During Fast Forest Floor Turnover in Montane, Temperate Forest Ecosystems, Frontiers in Earth Science, 7, 10.3389/feart.2019.00159, 2019.

Walker, J. C. G., Hays, P. B., and Kasting, J. F.: A negative feedback mechanism for the long-term stabilization of Earth's surface 600 temperature, J. Geophys. Res., 86, 9776-9782, 10.1029/JC086iC10p09776, 1981.

Weller, O. M., St-Onge, M. R., Waters, D. J., Rayner, N., Searle, M. P., Chung, S.-L., Palin, R. M., Lee, Y.-H., and Xu, X.: Quantifying Barrovian metamorphism in the Danba Structural Culmination of eastern Tibet, Journal of Metamorphic Geology, 31, 909-935, https://doi.org/10.1111/jmg.12050, 2013.

West, A. J.: Thickness of the chemical weathering zone and implications for erosional and climatic drivers of weathering and for carbon- 605 cycle feedbacks, Geology, 40, 811-814, 10.1130/g33041.1, 2012.

West, A. J., Galy, A., and Bickle, M.: Tectonic and climatic controls on silicate weathering, Earth Planet. Sc. Lett., 235, 211-228, http://dx.doi.org/10.1016/j.epsl.2005.03.020, 2005.

White, A. F. and Blum, A. E.: Effects of climate on chemical weathering in watersheds, Geochim. Cosmochim. Ac., 59, 1729-1747, http://dx.doi.org/10.1016/0016-7037(95)00078-E, 1995.

610   White, A. F., Bullen, T. D., Vivit, D. V., Schulz, M. S., and Clow, D. W.: The role of disseminated calcite in the chemical weathering of granitoid rocks, Geochim. Cosmochim. Ac., 63, 1939-1953, http://dx.doi.org/10.1016/S0016-7037(99)00082-4, 1999.

Williamson, M. A. and Rimstidt, J. D.: The kinetics and electrochemical rate-determining step of aqueous pyrite oxidation, Geochim. Cosmochim. Ac., 58, 5443-5454, http://dx.doi.org/10.1016/0016-7037(94)90241-0, 1994.

Yanites, B. J., Tucker, G. E., and Anderson, R. S.: Numerical and analytical models of cosmogenic radionuclide dynamics in landslide- 615 dominated drainage basins, J. Geophys. Res., 114, https://doi.org/10.1029/2008JF001088, 2009.